Bull Volcanol (2013) 75:765
DOI 10.1007/s00445-013-0765-7

RESEARCH ARTICLE

Sedimentology and geomorphology of the deposits from the August 2006 pyroclastic density currents at Tungurahua volcano, Ecuador

Guilhem Amin Douillet · Ève Tsang-Hin-Sun · Ulrich Kueppers · Jean Letort · Daniel Alejandro Pacheco · Fabian Goldstein · Felix Von Aulock · Yan Lavallée · Jonathan Bruce Hanson · Jorge Bustillos · Claude Robin · Patricio Ramón · Minard Hall · Donald B. Dingwell

Received: 21 January 2013 / Accepted: 20 September 2013 / Published online: 24 October 2013

Abstract The deposits of the pyroclastic density currents from the August 2006 eruption of Tungurahua show three facies associations depending on the topographic setting: the massive, proximal cross-stratified, and distal cross-stratified facies. (1) The massive facies is confined to valleys on the slopes of the volcano. It contains clasts of >1 m diameter to fine ash material, is massive, and interpreted as deposited from dense pyroclastic flows. Its surface can exhibit lobes and levees covered with disk-shaped and vesicular large clasts. These fragile large clasts must have rafted at the surface of the flows all along the path in order to be preserved, and thus imply a sharp density boundary near the surface of these flows. (2) The proximal cross-stratified facies is exposed on valley overbanks on the upper part of the volcano and contains both massive coarse-grained layers and cross-stratified ash and lapilli bedsets. It is interpreted as deposited from (a) dense pyroclastic flows that overflowed the gentle ridges of valleys of the upper part of the volcano and (b) dilute pyroclastic density currents created from the dense flows by the entrainment of air on the steep upper flanks. (3) The distal cross-stratified facies outcrops as spatially limited, isolated, and wedge-shaped bodies of cross-stratified ash deposits located downstream of cliffs on valleys overbanks. It contains numerous aggrading dune bedforms, whose crest orientations reveal parental flow directions. A downstream decrease in the size of the dune bedforms, together with a downstream fining trend in the grain size distribution are observed on a 100-m scale. This facies is interpreted to have been deposited from dilute pyroclastic density currents with basal tractional boundary layers. We suggest that the parental flows were produced from the dense flows by entrainment of air at cliffs, and that these *diluted* currents might rapidly deposit through "pneumatic jumps". Three modes are present in the grain size distribution of all samples independently of the facies, which further supports the interpretation that all three facies derive from the same initial flows. This study emphasizes the influence of topography on small volume pyroclastic density currents, and the importance of flow transformation and flow-stripping processes.

Keywords Tungurahua · Pyroclastic density currents · Flow stripping · Sedimentary wedge · Hydraulic jump

Editorial responsibility: V. Manville

G. A. Douillet (✉) · U. Kueppers · F. Goldstein · F. Von Aulock · Y. Lavallée · J. B. Hanson · D. B. Dingwell
Earth & Environmental Sciences, Ludwig-Maximilians-Universität, Munich, Germany
e-mail: g.douillet@min.uni-muenchen.de

G. A. Douillet · È. Tsang-Hin-Sun · J. Letort · J. Bustillos
Ecole et Observatoire des Sciences de la Terre, Université de Strasbourg, Strasbourg, France

G. A. Douillet · D. A. Pacheco · C. Robin · P. Ramón · M. Hall
Instituto Geofísico, Escuela Politécnica Nacional, Quito, Ecuador

G. A. Douillet · C. Robin
Institut de Recherche pour le Développement, UMR volcan, Quito, Ecuador

È. Tsang-Hin-Sun
Laboratoire de Géosciences Marines, Université de Brest, Plouzané, France

J. Letort
Laboratoire de Géophysique Interne et Techtonophysique (LGIT), Grenoble, France

Introduction

During explosive eruptions or upon catastrophic collapse of lava domes, density currents composed of clasts and gas flow down the volcanic edifice at hundreds of kilometers per hour, threatening the surrounding populations (Druitt 1996). Since direct observation is problematic, the understanding of such pyroclastic density currents (PDCs) represents a challenge whose solution is mainly based on analysis of deposit characteristics. Given the wide range of sedimentological patterns in PDC deposits, the parent flows are interpreted to have had a large range of solids concentrations (e.g., Sparks 1976), combined with different transport mechanisms (e.g., Burgisser and Bergantz 2002) evolving both spatially and temporally (Fisher 1983; Calder et al. 1997; Gardner et al. 2007). Here, we analyze the deposits of the pyroclastic density currents from the August 2006 eruption of Tungurahua volcano (Ecuador) in order to understand the origin and emplacement dynamics of the parental flows.

Conceptual models

Historically, pyroclastic deposits have been classified into three conceptual parental transport end-members: flow, fall, and surge (Sparks 1976; Wohletz and Sheridan 1979). Field observations however have revealed gradational deposit types (Valentine and Giannetti 1995; Wilson and Hildreth 1998; Sulpizio et al. 2008; 2010), which are thought to reflect different and transitional transport mechanisms (Burgisser and Bergantz 2002). Recent studies emphasize that deposits reflect only boundary layer processes during sedimentation and suggest a classification into "granular flow-", "tractional flow-" and "direct fallout-" dominated flow boundary end members (reviewed and conceptualized in Branney and Kokelaar (2002, p. 37–49)). For simplification, we use a threefold definition below: (1) massive, unsorted, and coarse-grained deposits are thought to reflect the absence of a basal tractional flow boundary during deposition, plus high particle concentration, and dominant particle–particle interactions in the parental flow (Brissette and Lajoie 1990; Boudon et al. 1993; Branney and Kokelaar 2002; Sarocchi et al. 2011). Where deposits are confined to topographic lows, the density (and solids concentration) of the entire parental flow is believed to have been high (Cole et al. 1998). We term this conceptual PDC-type "dense pyroclastic flow" in this study. (2) Cross-stratified and relatively finer-grained deposits are thought to form from turbulent flows with a basal tractional boundary layer and an important interparticle fluid presence with gas support (Crowe and Fisher 1973; Brissette and Lajoie 1990; Branney and Kokelaar 2002; Dellino et al. 2004). Such deposits are often found on interfluves and a lower density of the parental flows is inferred. Previously known as "pyroclastic surges" (Sparks 1976; Wohletz and Sheridan 1979), we term this conceptual PDC-type "dilute PDC" in this study. (3) We use the term "co-ignimbrite ash clouds" for dilute parts of the PDCs that are dominated by buoyancy. In such cases, even though the particles are gas supported during transport, no tractional flow-boundary zone is present because most momentum is transferred vertically and no consequent lateral currents are present (Talbot et al. 1994; Dellino et al. 2004). Thus, particles deposit by direct fallout and the associated sediment can be stratified, but not cross-stratified (Talbot et al. 1994).

The different PDC end-members can be present within the same flow as a basal dense pyroclastic flow and upper dilute PDC (Fisher 1995), vertically grading within a continuously density stratified current (Valentine 1987; Burgisser and Bergantz 2002), or evolve from one type to the other downflow (Gardner et al. 2007; Sulpizio et al. 2008; Andrews and Manga 2012).

Interaction with topography

Topography affects segregation mechanisms within granular flows (Baines 1998; Waltham 2004), determining threat for local populations in the case of PDCs (Fisher 1995; Abdurachman et al. 2000; Lube et al. 2011). Topographic separation into an upper, overflowing, less dense part and basal concentrated part is known as "flow stripping" in the case of turbidity currents (Piper and Normark 1983; Fildani et al. 2006). Branney and Kokelaar (2002) emphasize that "flow stripping" is preferable to "flow separation" because it does not imply two initially separate flows. Legros and Kelfoun (2000) analyzed momentum dissipation and showed that dilute PDCs may overflow topographic barriers with more ease than do dense flows. This is especially so for small volume PDCs, where a sharp interface between a basal dense pyroclastic flow and overriding dilute PDC is inferred (Fisher 1995; Takahashi and Tsujimoto 2000; Abdurachman et al. 2000; Saucedo et al. 2002; Cole et al. 2002; Charbonnier and Gertisser 2008). Takahashi and Tsujimoto (2000) showed that such dilute PDCs can travel independently of the main body, but their growth or waning depends on the supply of particles and gas from the main body, so they are no longer sustained and come to a stop after diverging from the course of the main body. Obstacles in a PDCs pathway also lead to partial diversion of dense flows in secondary "passes of saddles" (Branney and Kokelaar 2002). Lube et al. (2011) showed that the overflow of dense basal parts of the PDCs on interfluves at Merapi (Indonesia) was mainly controlled by three channel parameters: the cross-sectional area, confinement, and sinuosity.

Hydraulic jumps

A hydraulic jump is a sudden thickening and deceleration of a flow at the transition from supercritical to subcritical regime (Drazin 2002). Experiments on subaqueous, particle-driven, density currents showed that the coarse bedload deposits with the shape of a wedge at a break in slope due to a sudden decrease in shear velocity, possibly related to development of a hydraulic jump (García and Parker 1989; García 1993; Mulder and

Alexander 2001; Macías et al. 1998). Such "sedimentary wedges" (as defined in Sequeiros et al. 2009) are also observed in deep-sea turbidite fans (Prather 2003; Fildani et al. 2006). Within PDC deposits, lithic breccias emplaced at the base of a break in slope (Freundt and Schmincke 1985; Macías et al. 1998) or upstream obstacles (Freundt and Schmincke 1985) were interpreted to be the sedimentary signature of "pneumatic jumps" (the gaseous equivalent of a hydraulic jump, Branney and Kokelaar 2002, p. 18). At a metric scale, massive and unsorted stoss-depositional layers lying against the upstream face of buried buildings (Gurioli et al. 2002, 2007), or steep-sided truncations of pre-existing deposits (Schmincke et al. 1973; Freundt and Schmincke 1985; Giannetti and Luongo 1994) were interpreted as resulting from internal "pneumatic jumps" in density-stratified dilute PDCs. "Pneumatic jumps" triggered by cliffs are also supposed to be at the origin of co-ignimbrite plumes (Hoblitt 1986; Calder et al. 1997). These authors also noted that at a bend in the containing valley, an "ash cloud surge" overrode the channel and shortly after generating a buoyant plume.

Dune bedforms in PDCs

Dilute PDCs frequently deposit dune bedforms (DBs). Aggrading cross-stratified bedsets with up- or downstream migration of the crests are the most widespread internal structures observed (see Douillet et al. 2013 and references therein). However, controversies still exist on the interpretation of their fluid dynamical significance (Walker 1984; Sulpizio et al. 2008; Douillet et al. 2013). The size of DBs is usually observed to decrease with distance from the crater (Fig. 4 of Wohletz and Sheridan (1979); Fig. 8 of Druitt (1992)). In the 1965 Taal deposits, Moore (1967) reported DB wavelengths (length in our nomenclature) decreasing from 19 m in proximal areas to 4 m at 2.5 km from the volcano, the evolution occurring over the shortest distance where slope was acting against flow direction. Crests were aligned perpendicular to the flow direction. These size trends are sometimes related to an evolution of the outer bedform shapes and internal stratification patterns (Douillet et al. 2013 and references therein). Notably, dune-bedded deposits are also reported on levees and overbanks of turbidite-containing canyons (Normark et al. 2002; Fildani et al. 2006).

Tungurahua volcano and the August 2006 eruption

Tungurahua is an active andesitic stratovolcano (Hall et al. 1999) in the eastern Cordillera of the Northern Volcanic Zone in Ecuador (Hall et al. 2008). The present summit crater (5,023 m; base at 1,800 m above sea level (a.s.l.)) is breached to the northwest, directing lava flows and PDCs, together with the general westward wind direction for PDCs and ash clouds. In 1999, the volcano entered a period of activity with intermittent explosive phases and generation of PDCs. This activity poses a threat to many villages on the flanks, the city of Baños (25,000 inhabitants), the second largest hydroelectric dam in Ecuador and surrounding farmland (Samaniego et al. 2008). PDCs generated during a period of heightened activity in July and August 2006 reached populated areas, causing fatalities and severe damage to infrastructure and the agricultural sector (Barba et al. 2006; Kelfoun et al. 2009). The deposits of this eruptive episode are well studied. Kelfoun et al. (2009) mapped the deposits and numerically modeled the dense pyroclastic flows. Samaniego et al. (2011) presented a petrological description of the erupted products. Eychenne et al. (2012) analyzed the fall deposits associated with the August eruption, revealing a bimodal grain size distribution and suggesting that there was simultaneous deposition from the eruptive plume and co-ignimbrite ash clouds. Douillet et al. (2013) describe the dune bedforms deposited by dilute PDCs.

The August events began and ended with major fall events (Fide observatory-OVT staff). The eruptive column reached a height greater than 16 km, but did not collapse to form PDCs, which instead resulted from episodic destabilization of erupted material accumulated near the vent (Kelfoun et al. 2009). Several PDCs traveled down the northern, western, and southwestern flanks, controlled by the hydrological network to the base of the edifice (~1,800 m a.s.l.) where the deposits dammed the Chambo River for several hours (see map in Kelfoun et al. (2009)). The mean frontal velocity was estimated at 30 m/s using seismic data (Kelfoun et al. 2009) and the number of PDCs inferred to have passed through the study area (Fig. 1) was constrained to about five using monitoring data (e.g., Barba et al. 2006). The explosive event lasted for less than 8 h.

Kelfoun et al. (2009) mapped the deposits of the July and August eruptions and distinguished "dense flow deposits", mainly confined in the valleys, and "surge and fallout deposits" outcropping on the overbanks around dense flow deposits and on top of them (Fig. 1). In the lowermost zones of "los Pájaros" (Fig. 1), three depositional units were observed, the two basal units are coarse-grained and massive, and capped with a centimetric thick ash cover, the uppermost unit lacks any ash cover. Here, we present a sedimentological and geomorphological analysis of the deposits that reveals the transport and emplacement mechanisms of the August 2006 PDCs.

Facies associations

Nomenclature

In our field survey, we recognized three facies associations: "massive facies" (equivalent to "dense flow deposits" in Kelfoun et al. 2009), "proximal cross-stratified facies" and "distal cross-stratified facies" (later on, *Ma*, *P-Xst* and *D-Xst*, respectively).

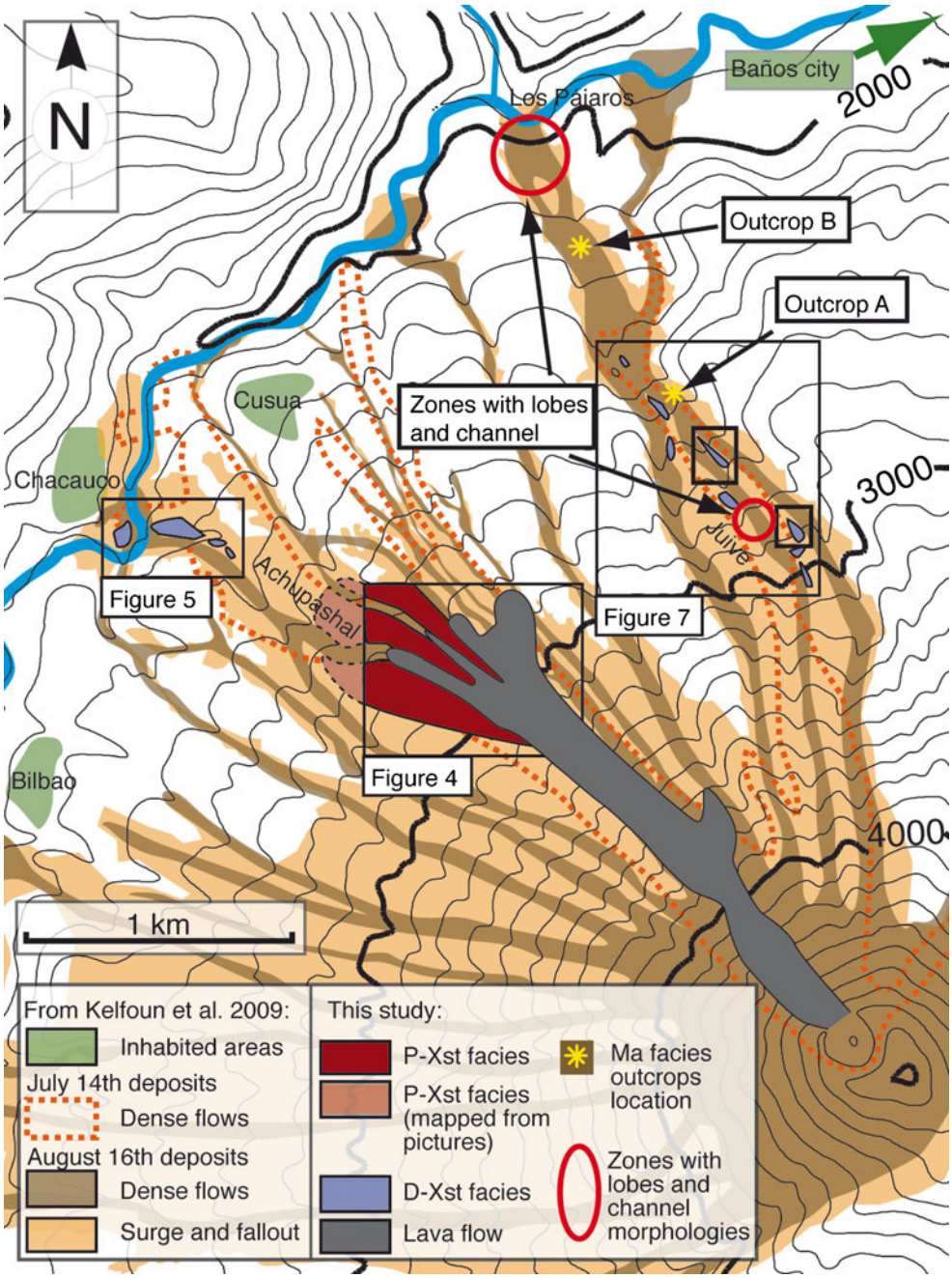

Fig. 1 General map of the deposits from the July and August 2006 eruptions of Tungurahua with "dense flows" and "surge and fallout" deposits modified from Kelfoun et al. (2009), "lava flow" modified from Samaniego et al. (2011) and Goldstein (2011), "*P-Xst*" and "*D-Xst*" facies from this study. Location of key features and outcrops are indicated

Planar stratified deposits identified as co-ignimbrite ash cloud deposits are not dealt with here. The *P-Xst*, *D-Xst* facies and co-ignimbrite ash cloud deposits of this study are all subdivisions of the "surge and fallout deposits" in Kelfoun et al. (2009). We use the term "facies" for deposits with common characteristic patterns. Facies includes lithofacies, spatial location, and geomorphic surface information. We term a millimeter-scale stratum a "lamina"; a "bedset" is a decimeter-scale group of laminae with similar structural characteristics. We use "layer" in order to avoid any genetic implication (such as implied in "unit") and it merely refers to an internally massive and thick (greater than centimeter-scale) stratum.

Fall deposits

The August eruptive period started and ceased with major ash and scoria fall. Field observations confirmed the presence of two thin, ashy layers at the base and top of the August deposits (outcrop A). The lower layer is approximately 1 cm thick and consists of fine ash with very porous clasts (up to 1 cm). The top August fall deposit is *ca*. 2 cm thick and made up of coarse ash and fine lapilli. The quasi-undisturbed nature of this final layer proves the excellent preservation state of the surface. The reader is directed to Kelfoun et al. (2009) and Eychenne et al. (2012) for details on the fall deposits.

Massive facies

The *Ma* facies is organized into multidecimeter-scale layers of massive and unsorted deposits of ash, lapilli and clasts of up to a few meters in diameter. It is mainly found confined to valleys of the drainage network and was partially eroded by the time we undertook our fieldwork (2009 and 2010). *Ma* facies deposits outcrop continuously from an altitude of ca. 3,800 m a.s.l. down to the base of the volcano at 1, 800 m a.s.l., where they spread and dammed local rivers for several hours (Barba et al. 2006). The thickness can reach tens of meters. Kelfoun et al. (2009) have interpreted this facies as deposits from dense pyroclastic flow. A maximum of six units corresponding to different PDCs or to pulses in a single flow were identified, but more might have occurred (Kelfoun et al. 2009).

Stratigraphic units

Two outcrops of *Ma* facies (A and B) from the Juive valley are described (Goldstein 2011) and have been sampled for granulometry (Fig. 2). They are both located downstream of the main ash deposition zones (see below; location in Fig. 1) in low-slope areas.

Outcrop A Outcrop A (Fig. 2a, b) is located 2.8 km from the vent, just upstream of the mouth of a steep-sided valley that confined the parent PDCs and downstream of a break in slope from 25° to about 13°. The exposure is 6 m thick and can be followed laterally for about 100 m parallel to the inferred parent flow direction. The top part (1.5 m) consists of sediments identified as reworked debris (lahar deposits), while the base corresponds to pre-2006 material, leaving 3.7 m of pristine 2006 deposit. Six individual layers (L1 to L6) were identified, described, and the matrix (taken as the fraction <2 cm) sampled for grain size analysis (Table 1).

Visual observation show that lithics are prominent in L1 (ca. 60 vol.%) but never reach more than 40 vol.% in other layers. This correlates with a smaller percentage of coarse material in the sieving results (Fig. 2c). In contrast, L2 to L6 are all matrix-supported and show similar componentry and grain size. Additionally, outcrop A is located at the runout limit of the July 2006 PDCs and an ashy layer is visible between L1 and L2 interpreted as representing a time between the flows that permitted deposition of a fall deposit by settling. The L1–L2 contact is interpreted as the record of the fall deposition at the beginning of the August events and L1 related to the July eruption, though it is unclear whether L1 represents a primary deposit or secondary lahar deposit.

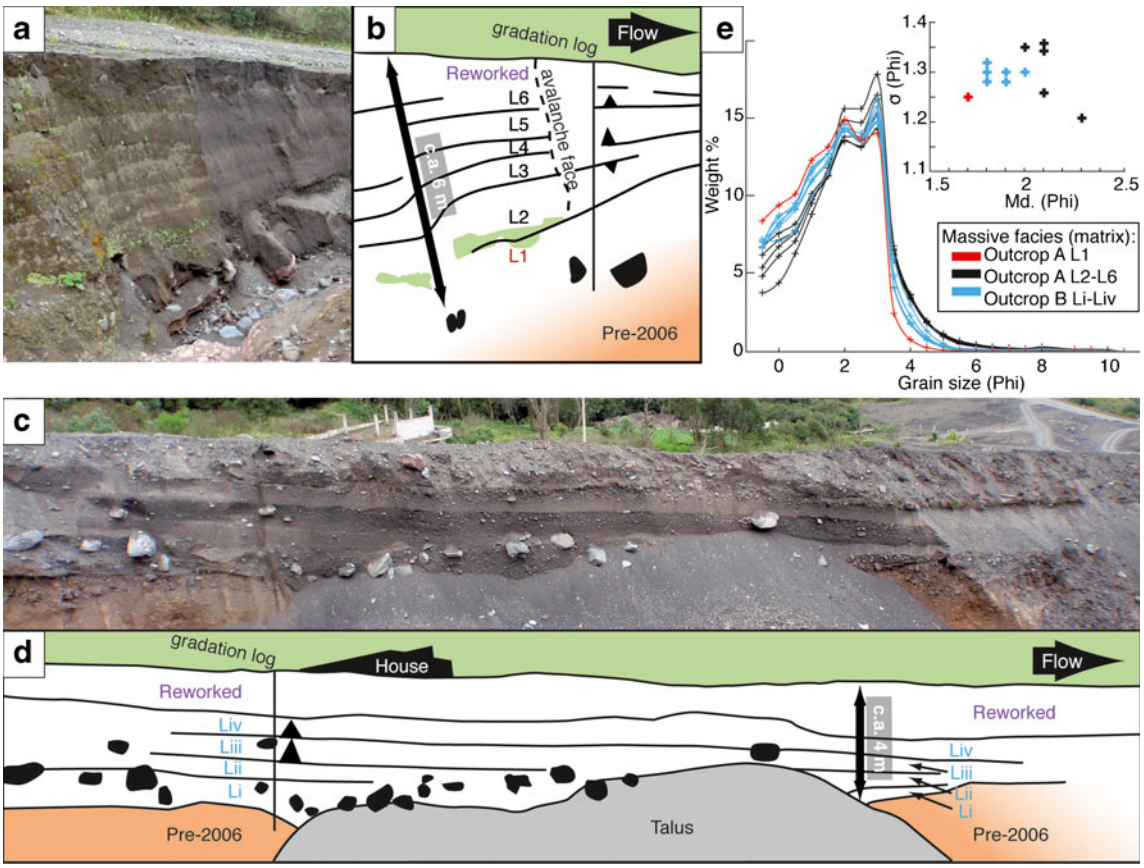

Fig. 2 Massive facies deposits ("Ma"). **a**, **b** Outcrop A; **c**, **d** outcrop B. The *sketches* emphasize layers and large clasts, and contain a scale, and *triangles* mark grading layers. **e** Grain size distribution of the different layers of outcrops A and B with median diameter versus sorting coefficient in *inset*

Table 1 Principal characteristics of the two massive facies outcrops

Layer	Organization	Thickness	Matrix (%)	Clast (%)	Clast size	Clast composition	Md (Φ)	Sorting (Φ)
Outcrop A								
TOP	Reworked debris (lahar deposits)							
L6–top	Inverse grading after 20 cm		60 %	40 %	Up to 20 cm			
L6–base	Normal grading in the basal 40 cm	L6 is >1.2 m	75 %	25 %	Average 4 cm		2.3	1.2
Border		*c.a.* 2 cm						
L5		40 cm	90 %	10 %	Up to 5 cm: matrix of ash and lapilli		2.1	1.35
Border		*c.a.* 1 cm						
L4	Quite homogenous	30 to 40 cm	90 %	10 %	Up to 7 cm; matrix of ash and small lapilli	Tabular clasts seem aligned with suspected flow direction	2.1	1.35
Border	Sudden decrease in clast >3 cm; possibly erosive, not planar							
L3–top	Upper 20 cm inversely graded	40 cm (could represent two independent layers)			1 to 8 cm	15 % red lithics; 35 % black porous scoria; 40 % black dense juveniles		
L3–base	Basal 15 cm similar to L2		75 %	20 %		<20 % lithics; mainly juvenile scoria	2.1	1.25
Border	Linear mossy vegetation growth on a competent protuding irregularity							
L2		50 cm	75	25	Up to 6 cm; mainly ranging 1–3 cm	<20 % lithics; mainly juvenile scoria	2	1.35
Border	Light gray ashy	*c.a.* 1 cm	-	-	<1 cm	Porous, fragile and not rounded		
L1	Border matrix/clast support	80 cm	40	60	Size up to 30 cm; 90 % between 1 and 10 cm	40–50 % colorful and dense (lithics)	1.7	1.25
BASE								
Outcrop B								
Top	Anthopogenic rubble material							
Liv–top			60 %	40 %	Up to 30 cm, average 8 cm		1.8	1.3
Liv–base	Coarsening up in clast concentration and size	>1 m	80 %	20 %	Up to 8 cm, average 4 cm		1.8	1.3
Border	Well defined ash layer							
Liii–top							1.9	1.3
Liii–base	Coarsening up by increase of clast concentration	90 cm			2 to 8 cm and some blocks		1.9	1.3
Border	Contact seems not erosive, following the top of Li							
Lii		80 cm	80 %	20 %	Lapilli range	Mainly angular juvenile clasts	1.9	1.3
Border	Contact seems not erosive, following the top of Li							
Li	Fills underlying depression. Presence of blocks up to 1.5 m diam.	>90 cm	60 %	40 %	4 to 7 cm		2	1.3
BASE	Soil with pre-existing depressions. The contact contains vegetation and is thus not erosive							

Outcrop B Outcrop B (Fig. 2d, e) lies ca. 1.1 km downstream of outcrop A, in an area where the parent PDCs were not confined by topography. The visible exposure has a total length of about 30 m in the downslope direction. Total thickness varies from 3 to 5 m where a depression is filled with deposits. The base is marked by sediments with a reddish color containing roots and is interpreted as the pre-2006 paleosol. The top is covered with anthropogenically reworked material. Four layers are recognized in the 2006 deposits. Large clasts are distributed throughout the outcrop (16 clasts >0.5 m; largest ca. 1.5 m). Layers 1 and 2 were sampled once; layers 3 and 4 were sampled at their base and top since they showed inverse grading.

"Pancake-lobes"

The surface of the *Ma* deposits locally exhibits a fingered lobe-and-channel morphology (Fig. 3a). The lobes strictly follow topographic lows on the surface of earlier deposits

and build up with a droplet-like morphology: a concave upper surface upstream, ending in a convex morphology, with steep fronts and sides. Upstream from the terminal lobes, only the side levees record the path of the flows (Fig. 3b). They have been observed on the steep slopes of the Chontal sector as well as on low slopes in the distal parts of the Juive valley (Fig. 3a).

The surface of the lobes and levees contains numerous large clasts (>6.4 cm diameter). We termed "pancakes" large clasts characteristically flat and disk-shaped (length and width are about five times the thickness) with a bread-crusted texture (Fig. 3c). The inner part of the pancakes is rich in spherical or elongate bubbles, whereas the rim is denser, sometimes glassy, and shows deep cracks (Fig. 3c). These oblate and fragile pancakes are sometimes intensely folded, but are found unbroken more than 6 km away from the vent, on the lobe and levee surfaces.

Measurements of the long, intermediate, and short axes were performed for all large clasts encountered on three parts of a lobe: on the side, upper surface, and at a depth of about 40 cm below the surface (Fig. 3d). The maximum projection sphericity (Sneed and Folk 1958) was calculated:

$$S = \left((dS\text{^}2)/\left(dL * dI\right)\right)\text{^}(1/3)$$

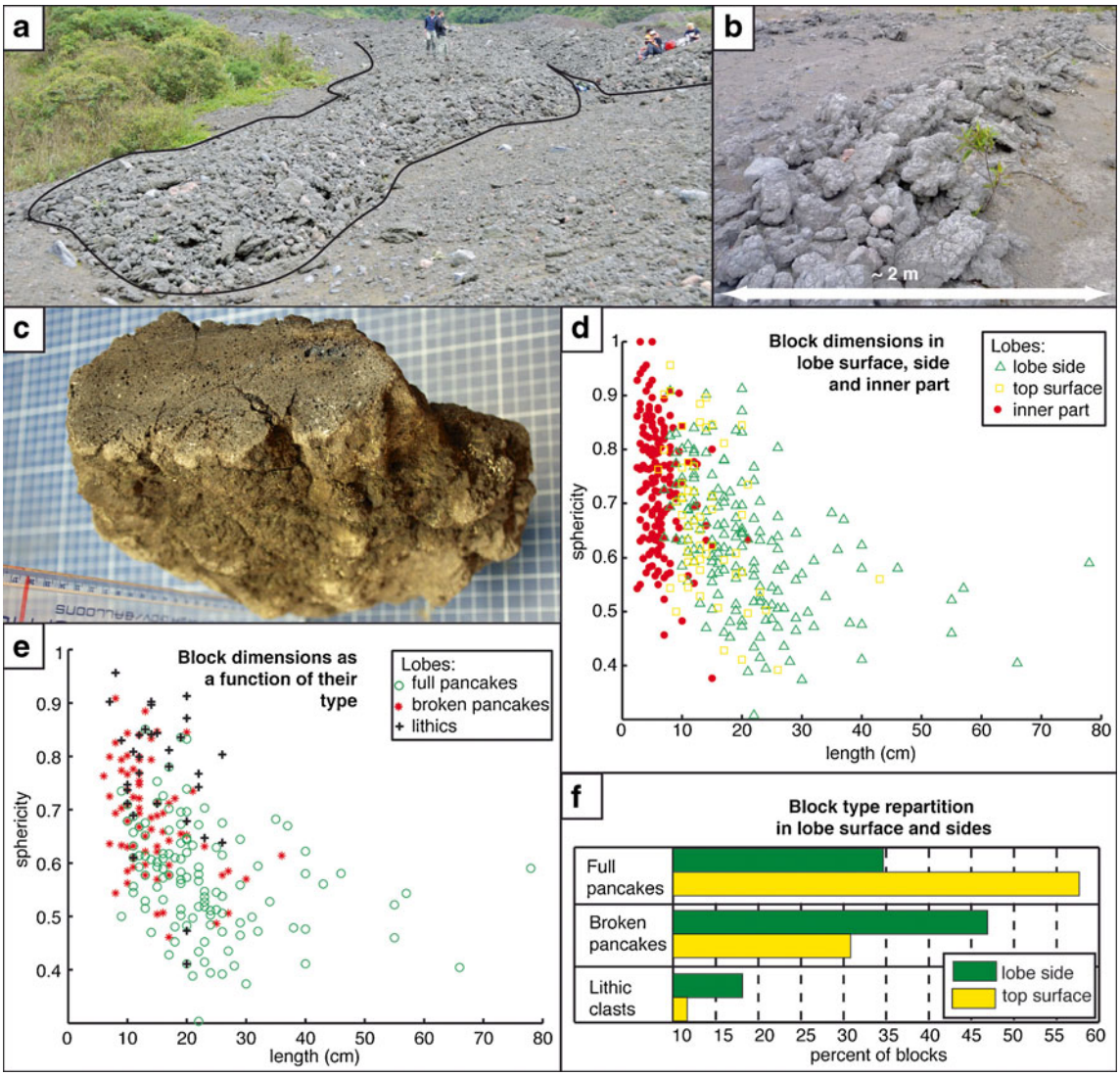

Fig. 3 Lobe and cleft morphologies at the surface of the massive facies. **a** A terminal lobe, geologists in the background for scale. **b** Marginal levée containing "pancakes". **a**, **b** Location in Fig. 7. **c** Cut though a "pancake", background scale and vertical scale marked in cm, the red line marks 26 cm height. **d** Length versus sphericity plot of clasts encountered on a lobe. **e** Length versus sphericity plot of clasts encountered at the surface and side of a lobe versus their type. **f** Relative proportions of full "pancakes", broken pieces of "pancakes" and lithic clasts on the side and top surface of a lobe

With dS the short axis; dI the intermediate axis and dL the long axis.

Large clasts on the lobe sides are the most flattened and longest, whereas the inner lobe contains the smallest and most spherical ones (Fig. 3d). Distinction between large clasts identified as full pancakes, broken pancakes, and lithics was made in the field on lobe upper surface and flanks (Fig. 3e, f). Both parts contain a majority of juvenile pancakes and few lithics, but the upper surface is made of a majority of full pancakes, whereas the flanks contain more broken pancakes. Full pancakes are flatter than the broken pieces, but lithics show the most spherical shapes (Fig. 3e).

Cross-stratified facies

Two types of "cross-stratified facies" (*Xst*) are recognized in the deposits: (1) the proximal facies (*P-Xst*) on the steep upper slopes, where the valleys of the drainage network are not sharply defined (Fig. 4) and (2) the distal facies (*D-Xst*) where valleys are deeply incised (Figs. 5, 6, 7, 8, and 9). Both are predominantly composed of ash and are well stratified with abundant cross-stratification, although massive, decimeter-thick lenses, sometimes with fining-upward trends are present (Figs. 4c and 8f). These massive layers in places grade into diffusely to crudely stratified laminae and vice versa. These deposits occur on the overbanks of the valleys containing the *Ma* facies. Their surfaces reveal well-developed, meter-scale dune bedforms (DBs; Figs. 4b, d and 8e), whose shapes and structures are detailed in a companion paper (Douillet et al. 2013). They vary from 1 to 20 m in length and 0.1 to 2 m in thickness. A 2 cm thick fall deposit was observed draping the DBs, testifying to their pristine shape. Internally, the DBs exhibit cross-stratification patterns typical of PDC deposits, mainly aggrading and stoss-depositional structures (e.g., Schmincke et al. 1973; Cole 1991). Cut-and-fill structures occur locally. No ripple beds, soft sediment deformation structures, or overturned beds have been observed. Partially carbonized wood fragments are present in places. Apart from these characteristics, the two types of *Xst* facies show different patterns in their overall architecture and types of sedimentary structures that justify their distinction.

Proximal cross-stratified facies

The *P-Xst* facies mainly exhibits long (3.2–17.5 m) but not very broad (2.4–12 m) elongate DBs with diffuse crests producing only a slight bulge on the surface (Fig. 4b). They have poorly defined transverse shapes and are widely separated (>20 m). Internally, DBs exhibit thick (up to 20 cm), stoss-constructional, lensoidal layers of a massive mixture of ash, lapilli, and isolated large clasts <10 cm diameter (Fig. 4d). These patterns alternate with thin (1–2 mm) and finer-grained (mainly ash) laminae forming aggrading bedsets with an upstream migration of the crests locally grading into massive ashy layers and vice versa (Fig. 4c). The DBs are interpreted to have formed from high capacity and competence currents and produced at the transition between granular- and tractional-dominated boundary zones by topographic blocking of the bedload (Douillet et al. 2013).

Adjacent eucalyptus trees (15–30 cm diameter) have lost their bark and exhibit 3-cm-deep dents (Fig. 4b). Only minor charring is visible above the deposits, but significantly carbonized parts are found buried in the deposit. In areas near the *Ma* facies, trees are broken, some above their roots (covered in the deposits), others above the surface of the deposits (Fig. 4a). Outside the area of highest impact, trees are still standing but dead.

Distal cross-stratified facies

In comparison with the *P-Xst* facies, the *D-Xst* facies is much poorer in coarse clasts and primarily composed of ash with a subordinate fine-lapilli component distributed throughout in the ash or grouped in decimetric-thick lenses (Fig. 8f). No agglomeration structures are observed and low moisture content of the fluid phase is inferred. Several isolated deposition zones of *D-Xst* facies were observed along a single valley but in restricted areas (Figs. 5, 6, 7, 8, and 9).

DBs are much steeper-sided than for the *P-Xst* facies and an evolution of their morphology is observed (Douillet et al. 2013). The largest ones have transverse shapes, reaching lengths of 17 m. Smaller DBs can show lunate shapes (crests concave upstream), as noted by Sigurdsson et al. (1987) at El Chichón (México). On outer edges of the deposition zones, DBs tend to be very short but wide, more symmetrical, and organized into trains, and are thus termed "two dimensional". Internally, and contrarily to the *P-Xst* facies, cross-stratification exclusively consists of crude millimeter-scale laminae organized in stoss-aggrading bedsets, locally grading into diffusely stratified to massive and vice versa. They are interpreted as having formed under the influence of both direct fallout and traction-dominated boundary layer flows (Douillet et al. 2013).

Spatial distribution

Mapping method

The *Xst* deposit distribution was mapped with a handheld GPS along the two valleys most affected by PDCs, the Juive and Achupashal valleys (Fig. 1). In areas containing abundant DBs, the orientation, and sometimes length, thickness, and width of several hundred DBs were measured (Figs. 4a, 5a, 6, and 8). The direction of the parent currents was inferred assuming that DB crests are oriented perpendicular to the flow direction (as observed by Moore (1967) at Taal). Although

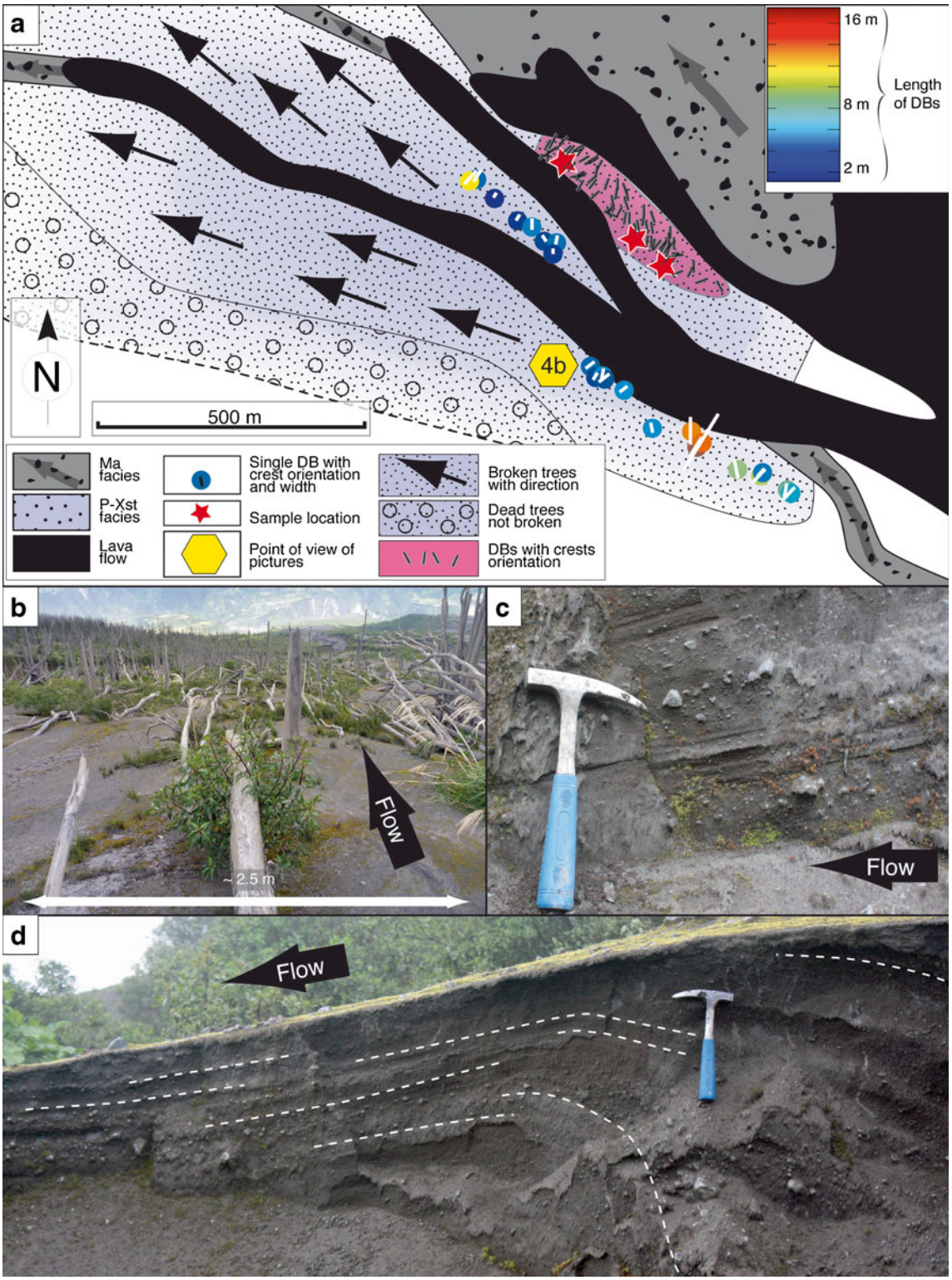

Fig. 4 Proximal cross-stratified facies in Achupashal valley. **a** Map of the deposits with DB orientation, length and width, direction of fallen trees, and extent of damaged trees. **b** Trees are broken and align in the downstream direction. **c** Variation in sedimentological patterns within a proximal DB. **d** Cross-section of a DB from proximal zone

outer shapes only reflect the final stages of a DB's formation, cross-sections show general stability of the DB crests throughout deposition.

Color-coded isopach maps of the dimensions of the DBs were produced using Matlab™. Linear interpolation was done by Delaunay triangulation, connecting each data point to its

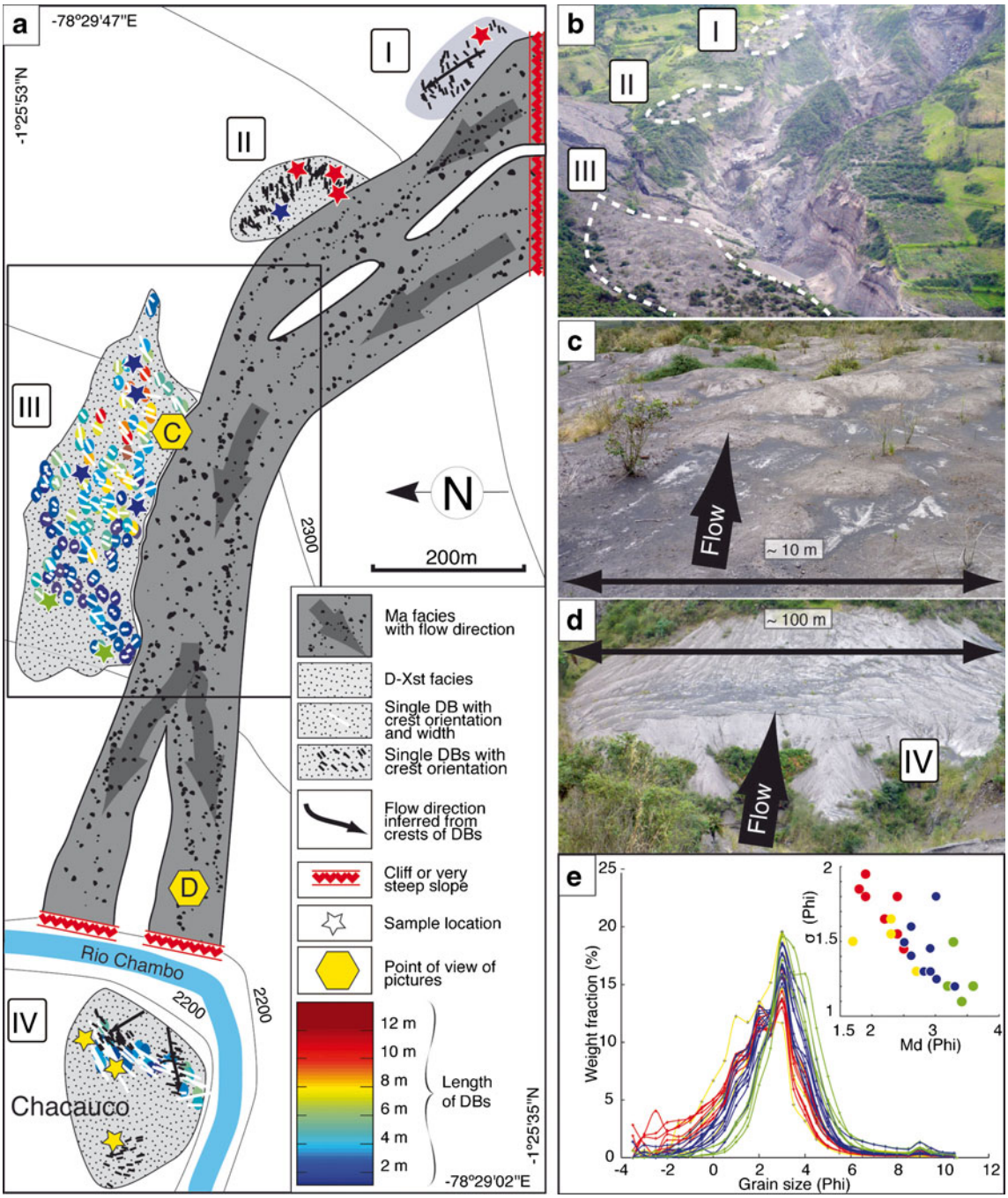

Fig. 5 Distal cross-stratified facies in Achupashal valley. **a** Map of the deposits with DB orientation, length and width. **b** Photograph showing ash bodies I, II, and III. **c** DBs at the surface of ash body III. **d** Ash body IV, note wide but short DBs on the surface. Points of view of pictures are marked on the map. **e** Grain size distribution of the distal Achupashal samples. *Inset* shows median diameter versus sorting coefficient. Sample location on map (*stars*). Note downstream fining

natural neighbor and the Voronoi polygon around each resulting point was plotted with color coding (Sandwell 1987; Barber et al. 1996). This method was preferred to a kriging because the variogram or expectation of the data is unknown but the data are reliable (Cressie 1993). The density of polygons reflects the density of data and the lines representing the crests of DBs have a width proportional to those of the DBs (Figs. 4a, 5a, 6, 7, and 8a, b).

Proximal cross-stratified deposits: the upper Achupashal valley

The *P-Xst* deposits in the Achupashal valley are found below 3,100 m a.s.l. (3.1 km from the crater rim) at a general decrease in slope angle (from 30° to 25°; Fig. 1), where the drainage network is not as sharply defined as lower down. The deposits outcrop on the overbanks of the valleys in a sheet-like

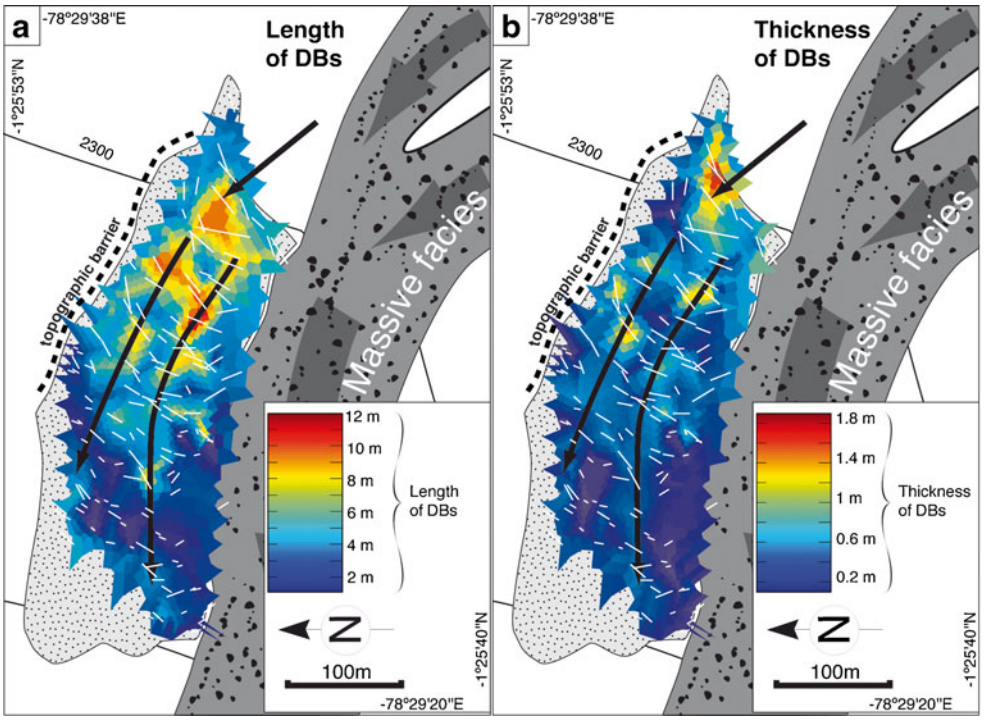

Fig. 6 DB dimensions on ash body III. *White lines* mark the crests of DBs with their orientation and the length is proportional to the width of the DBs. *Arrows* mark the inferred flow direction

fashion (c.a. 2×1 km^2; Fig. 4a), which gradually thins from a minimum of 5.5 m (base not observed) in central zones, until it eventually vanishes laterally.

Fallen tree tops align in a direction thought to reflect the parent flows' direction (Fig. 4b), but show less variation in orientation than the DBs. Crest orientation of DBs are subparallel to the valleys and follow the main gradient, though DBs closest to the *Ma* facies deposits are oriented perpendicular to the valleys.

Distal cross-stratified ash bodies

In distal zones, well-developed drainage channels directed PDCs. Whereas *Ma* facies deposits are confined to the valleys, the *D-Xst* facies is organized as several spatially isolated and disparate "ash bodies" (Figs. 5, 6, 7, and 8). By ash body, we mean a significant volume of *D-Xst* facies deposits distributed over a restricted area, regardless of its genesis. The main characteristics of each ash body are listed in Table 2 for the distal Achupashal valley and Table 3 for the Juive drainage network. They often show a sedimentary wedge shape, i.e., a sharp increase in thickness at the upstream end, and a gentle decrease downstream (Fig. 9a). This wedge shape onset is best shown by ash body C (Fig. 8), where it takes the shape of a quarter pipe, 82 m in width, that thickens from 0 to 5.5 m over less than 14 m in the flow direction (Fig. 8c, d). There, DBs' orientation radiate from the quarter pipe and have crests normal and in train with it near the onset (Fig. 8a–c). In sedimentary wedges, DBs decrease in size downstream.

Granulometry and componentry

Methods

Samples were collected in August 2009 for granulometry. For the *Ma* facies, the <2 cm fraction was sampled in each layer from outcrops A and B (10 samples; Fig. 2). Thirty-five samples were taken on the stoss and lee sides of DBs: 6 in the *P-Xst* facies, 26 in the lower Achupashal and 3 in the Juive valley (location Figs. 4a, 5a and 7, respectively). For those in DBs, the top 5 cm were removed prior to sampling in order to exclude the final fallout deposits and reduce weathering and modification effects from wind and precipitation.

Mechanical sieving (10 min, 0.5 Φ interval between −3.5 Φ and +3 Φ) was performed on dry aliquots of 250 and 75 g for the *Xst* and *Ma* facies samples, respectively. The fine fraction (+3.5 to +10.5 Φ) was measured by laser diffraction in a LS230 (Beckman-Coulter, 5×5 runs of 0.1 g averaged). The data were merged to produce a single continuous curve, with cumulative percent of material (<3.5 Φ) in the laser data corresponding with the mechanical one (Fig. 10a, c, e).

The results were interpolated ("interp1–pchip option" in Matlab™) and integrated to obtain cumulative curves, and compute the mean grain size (M_d) and sorting coefficient (σ) (Otto 1939; Fig. 10a, c, e):

$$M_d = \Phi_{50}; \sigma = (\Phi_{16} - \Phi_{84})/2;$$

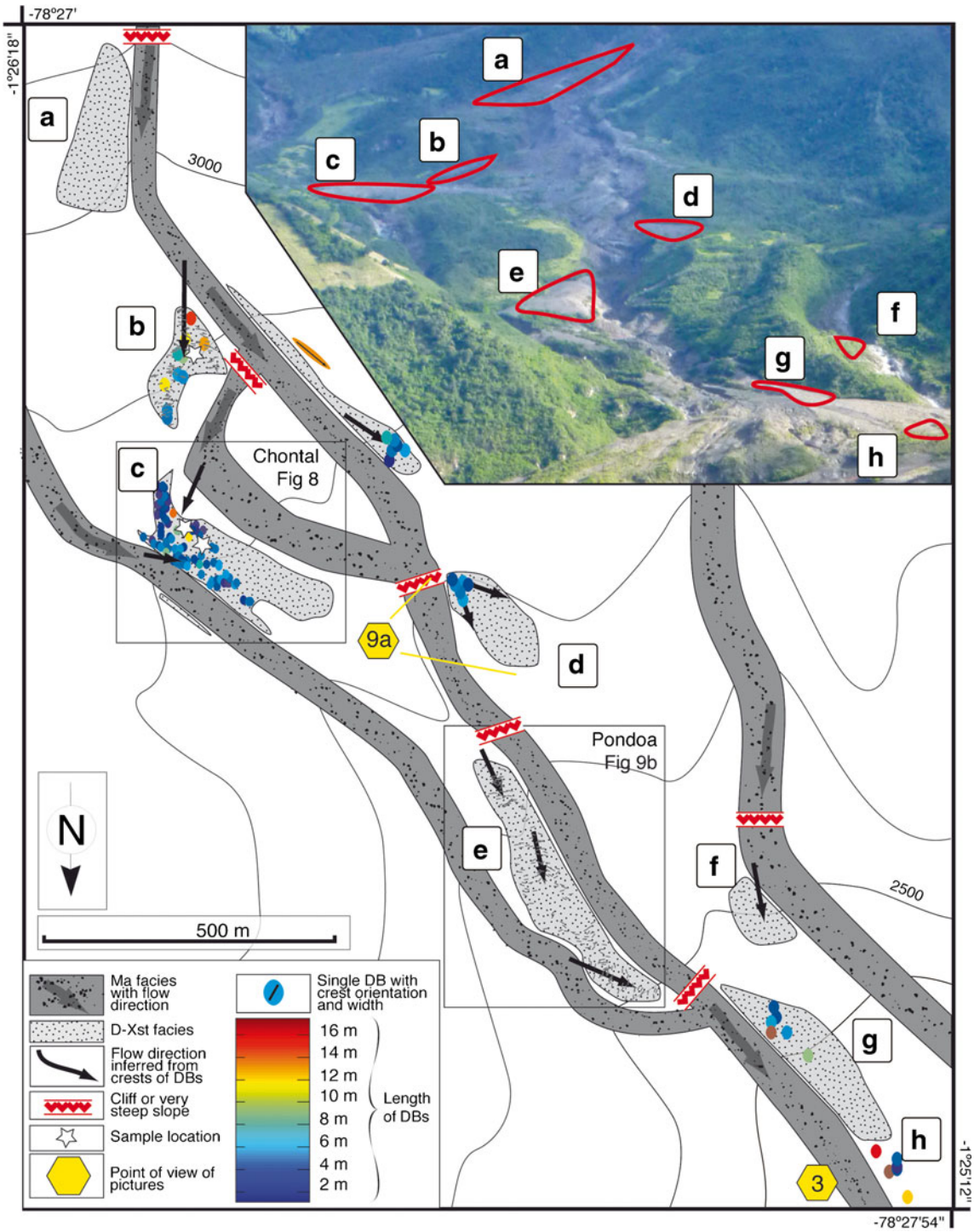

Fig. 7 Map of the Juive drainage with DB orientation, length, and width. In inlet is a photograph of the zone. *Rectangles* surround the map of Chontal (Fig. 8a, b) and Pondoa (Fig. 9b)

where Φ_i is the grain size for which i% of the total material is smaller than the given grain size.

Componentry analysis was performed on the 0 Φ (1 mm) fraction of c.a. 16,000 clasts from five samples with four groups defined: crystal fragments, altered, vesiculated, and dense clasts (Fig. 10f).

Results

The occurrence of three modes at 1, 2, and, the main one, at 3 Φ independently of the facies is striking in all samples (Fig. 10a, c, e). At outcrop A, the matrix of L1 was found to be coarser than in L2–L6, the latter being all very similar

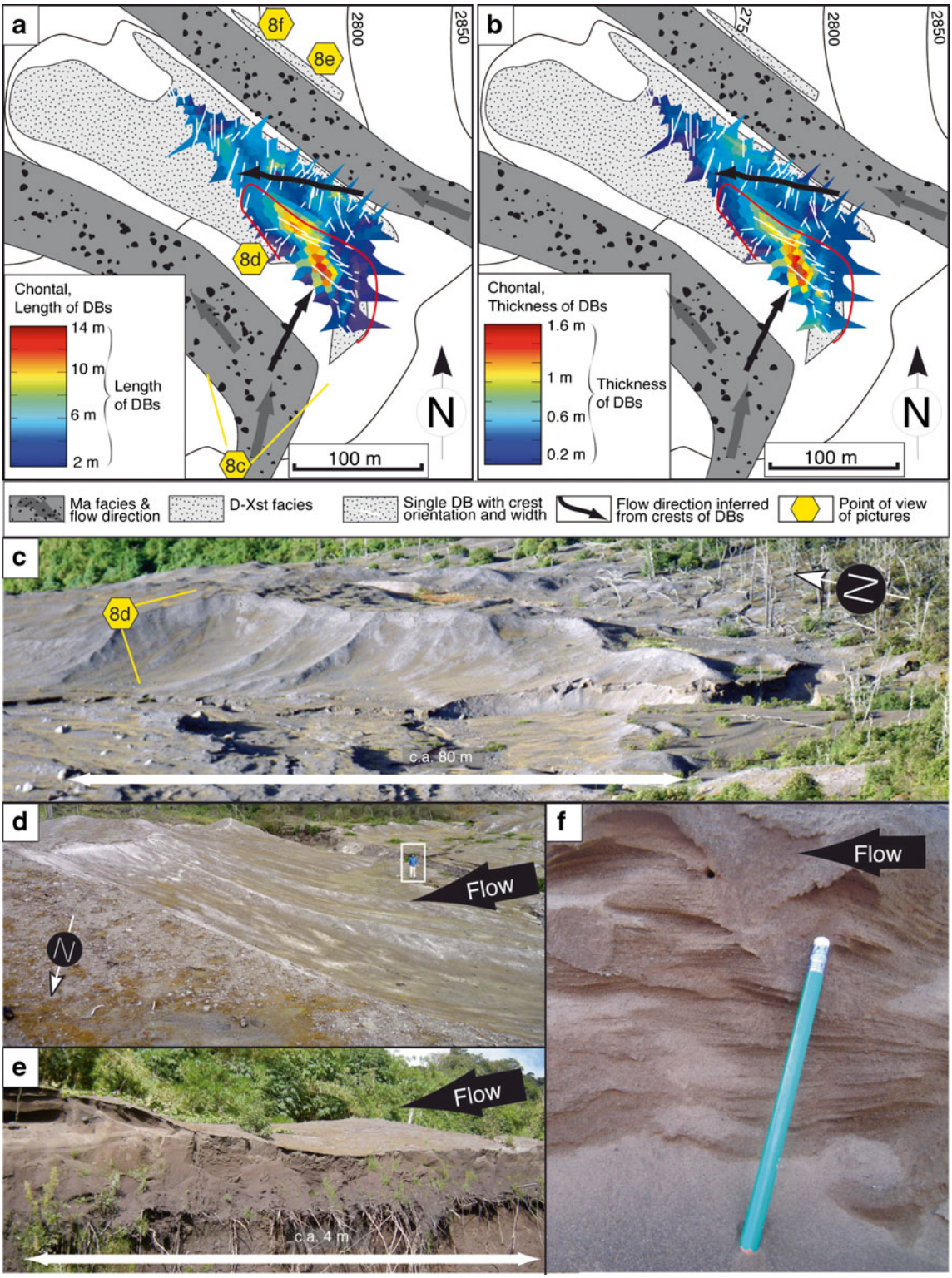

Fig. 8 Distal cross-stratified facies in Chontal sector. **a**, **b** DB dimensions; *white lines* mark the crests of DBs with their orientation and the length is proportional to the width of the DBs. *Arrows* mark the inferred flow direction. **c**, **d** the sudden quarter pipe shape of the western upstream side of the ash body. **e** DBs on the edge of the ash body. Note vegetation at the basal contact between the deposit and underlying soil. **f** Ash cross-stratifications in the Chontal sector

(Fig. 2c). This confirms the particularity of L1 from field observation (higher clast content and size; Fig. 2c). The matrix of the four layers from outcrop B exhibit very similar grain size distributions between each other and contain less material

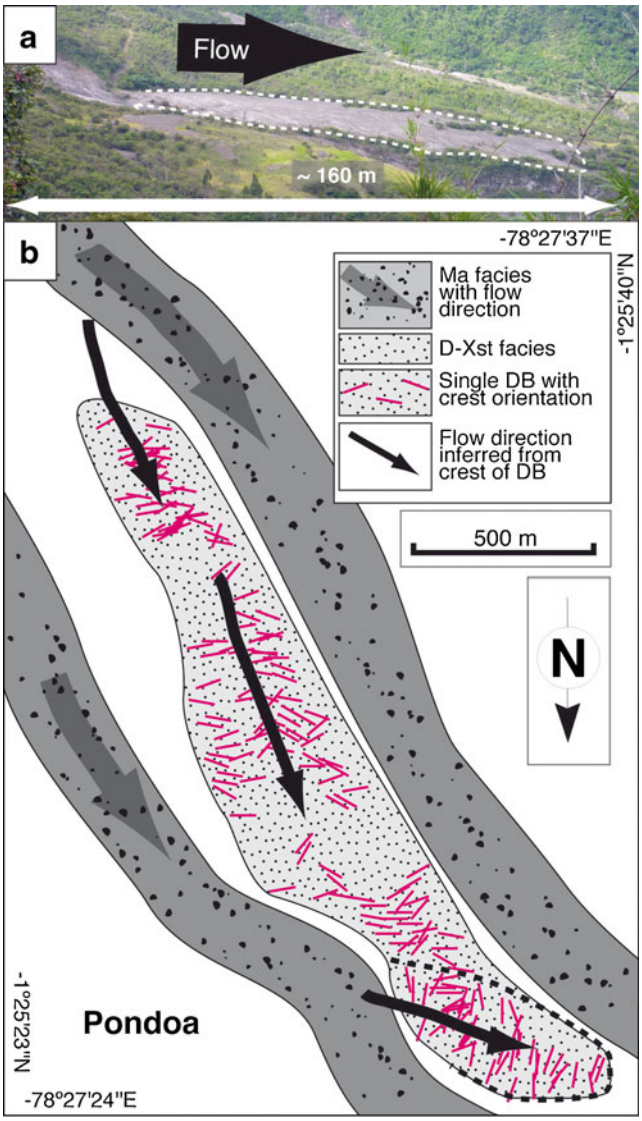

Fig. 9 Ash bodies within the Juive drainage. **a** Ash body D downstream of a cliff, picture location in Fig. 7, looking westward. **b** Map of ash body E with DB orientation. The influence of two currents is visible by the orientation of the dune bedforms and the eastern valley influence zone is underlined by dashed line

<1.5 Φ and finer M_d compared to outcrop A (Fig. 2c). No correlation between layers from the two outcrops could be done, but L1 from outcrop A seems absent in outcrop B. Samples from the matrix fraction of the *Ma* facies show better sorting (probably due to the cutoff at 2 cm) but a coarser content relative to the *Xst* samples.

Samples from *P-Xst* and *D-Xst* facies are similar, poorly sorted (following the verbal classification of Folks 1964, i.e., 1 Φ<σ<2 Φ) with M_ds between 1.8 Φ and 3.7 Φ (Fig. 10b). In a M_d vs σ graph, they plot within the flow field described by Walker (1971), but not in the most probable zone. They also partially overlap with the fall field (Fig. 10d) and fit very well with the "base-surge field" defined by Crowe and Fisher (1973; Fig. 10d), even if Walker (1984) showed that large variations in the grain size parameters of pyroclastic cross-bedding occur.

Samples from the lower Achupashal valley show a downstream fining between ash bodies I, II, and III (green, pink, and black, respectively, in Fig. 5e). Samples from ash body IV (the lowermost deposit) are rather similar to the *P-Xst* samples, as also observed in the field, and interestingly, ash body IV is located at the base of a cliff.

Componentry was performed on samples from the *P-Xst* zone, ash bodies II, III, and IV in the lower Achupashal and ash body B in the Juive drainage (Fig. 10f). Two samples differ significantly from the average results (57 wt.% vesiculated, 19.5 wt.% dense, 12.5 wt.% crystal, 11 wt.% altered): the *P-Xst* sample reveals less vesiculated (38.5 %) and more dense non-altered clasts (35.1 %) and crystal fragments (17.1 %). The sample from ash body B shows more vesiculated (69 %) and less dense clasts (7.9 %).

Dynamic repose angle (the slope of a heap constructed by falling material) and static repose angle (the slope of a heap under excavation) are 32° and 41°, respectively, for bulk *D-Xst* samples and 38° and 52°, respectively, for the fine fraction (<250 μm).

Interpretation

Facies

Massive facies

Ma facies is massive and unsorted, contains large clasts, is coarse grained, and deposits are confined by topography, respectively, indicating that there was no traction-dominated flow boundary zone and that the parent flows had a large transport capacity and were too dense or thin or slow to overflow topography. *Ma* facies is interpreted as the deposits of parental dense pyroclastic flows. The different layers, in places separated by thin strata of ash interpreted as fall deposits, are the results of different flows separated by pauses. The report from direct observation of three main flows in this valley contrasts with the six layers observed at outcrop A and four at outcrop B, and we infer that some flows did not reach the lowermost parts of the valley. Predominance of lithics, smaller percentage of coarse in the sieving results, together with the location of outcrop A at the runout limit of the July PDCs and the ashy layer between L1 and L2 (interpreted as a time break in the flow), suggest that L1 was formed during the July eruption, though it is unclear whether L1 represents a primary deposit or secondary lahar debris deposit. The L1–L2 contact is thus interpreted as a fall deposit formed at the beginning of the August events.

The lobes and levees formed during the last flows reported from direct observation. They indicate self-channelization of

Table 2 Principal characteristics of the distal ash bodies from the Juive valley

Ash body	Location	Shape	DBs dimensions (max, min, mean)	DB type (see Douillet et al. 2013)	DBs orientation	Notes
Juive drainage network						
A	3.6 km from the vent; downstream cliff; steep slope (25°)	Fan; The thickness of the body is maximal in the central part and decreases toward the edges		Mainly transverse	Subparallel to valley before the bent, some DBs close to the valley are perpendicular to it	
B	Outer overbank of valley curve (from N0 to N330); steep slope (22°); elevation: 2,900–2,870 m.a.s.l.	Downstream decrease in DBs' dimensions	Width: (41×4×13.34); length: (14.8×5.7×9.34); thickness: (20.2×0.94);	Transverse; 2D	Subparallel to valley before the bent	
C/Chontal	On the outer overbank of two bordering valleys that curve; elevation: 2,843–2,772 m.a.s.l.	Sedimentary wedge; quarter pipe onset from the West; downstream decrease in DBs' dimensions;	Width: (18.5×1.4×6.40); length: (14×1.5×4.9333); thickness: (1.6×0.1×0.57);	Transverse at onset; lunate; 2D on edges; found without DBs in lower part (in Nov. 2010)	Subparallel to valleys before the bent; radiating from western quarter pipe. Crest orientation and size decrease of DBs show that currents from both valleys influenced the morphology;	Main input of sediment seems to come from western valley. Basal and downstream parts contain an increased amount of coarse, and it seems that Ma facies is present, though clearly absent on the edges (Fig. 8e).
D	Downstream cliff	Sedimentary wedge		Transverse; lunate	Subparallel to valley and opening angle (N340 to N290–valley N340)	
E/Pondoa	Downstream cliff	Elongate			Their orientation shows that the ash body was emplaced by currents overflowing from a curve higher in the valley (Fig. 9b). Orientation of DBs in the lower part of this zone is also influenced by currents coming from the eastern valley	
F	Downstream steep slope outer overbank of valley curve	Fan				
G	Downstream steep slope; behind topographic shield;					
H	6 km from vent; elevation: 2,040–2,025 m.a.s.l.	Not an ash body form	Width: (14×6.2×10.26); length: (17.3×2.5×9.5); thickness: (1.5×0.3×0.78);	Numerous composite DBs (climbing on each other)		

the parental flows, implying an upper free boundary and a dense and steady-state frictional regime (Félix and Thomas 2004). The higher amount of large clasts on levees and lobes surface compared to the inner part is commonly observed (Cole et al. 2002; Félix and Thomas 2004; Lube et al. 2007) and interpreted as due to rafting of coarse clasts to the front and sides of the flow (Calder et al. 2000). Indeed, the disk-shaped "pancakes" cannot be preserved over 6 km of transport in the inner part of a flow: size measurements show an absence of full pancakes inside the lobes. This further indicates a sharp density interface at the upper boundary of the dense pyroclastic flows producing the lobes.

As commonly observed in other deposits of dense pyroclastic flows (e.g., Boudon et al. 1993), outcrop A deposits (more upstream) contain fewer large clasts as well as finer-grained matrix than outcrop B deposits, indicating a bypass at outcrop A before deposition of the large clasts at outcrop B, and a lower carrying capacity at outcrop B.

Proximal cross-stratified facies

The broken trees and flatness of bedforms indicate the high energy of the parental flows. This facies shares similarities in its architecture with the "veneer and surge overbank facies"

Table 3 Principal characteristics of the distal ash bodies from the Achupashal valley

Ash body	Location	Shape	DBs dimensions (max, min, mean)	DB type (see Douillet et al. 2013)	DBs orientation	Notes
Lower Achupashal valley						
I	6.4 km from vent; downstream major cliff; behind a topographic shield		Width: up to 15 m; length: up to 12 m; thickness: up to 1 m;	Mainly transverse	Subparallel to valley before the bent	
II	Very close to valley			Mainly transverse	Initially out of the valley but towards the valley downstream	Local topography strongly dips toward the thalweg
III/Cusua	Outer overbank of valley curve elevation: 2,325–2,187 m.a.s.l.	Sedimentary wedge; large DBs hilight the onset and decrease in dimensions downstream	Width: (17.5×1.4×4.75); length: (12×1.1×4.56); thickness: (1.9×0.1×0.51);	Transverse; lunate; 2D on edges	Concentrically to upstream onset; subparallel to valley before the bent on upstream half; following gradient on lower part with possible splitting of the current (from orientation and size)	An abandoned house 50 m away from the ash body was almost completely preserved and only a few centimeters of ash entered it
IV/Chacauco	Downstream cliff; base of the volcano; on the opposite side of Chambo river (western side), dip against flow dection (-10º); elevation: 2,166–2,156 m.a.s.l.	Fan (Fig. 5d)	broad but short (Fig. 5d) width: (38×5.2×13.06); length: (6.2×1.84); thickness: (1.1×0.3×0.53);	Only 2D	Concentric to the eastern valley branch from Achupashal before cliff (Fig. 5a)	Direct observations: PDCs crossed the Chambo river and most material landed into it; steam and ash clouds billowing from the river. Field observations show an increased amount of coarse, comparable to P-Xst facies

described by Lube et al. (2011) for Merapi volcano. However, cross-stratification is more abundant at Tungurahua. Moreover, the location of overbank deposits with orientation of DBs pointing away from valleys do not support interpretation as a veneer flow deposit in the sense of Walker et al. (1981) as "the record of the passage of a pyroclastic flow, where the flow itself has moved farther on", since no flow has moved farther on in the direction indicated by the orientation of the DBs.

The *P-Xst* facies contains features indicating deposition from two alternating processes. The ashy bedsets evolving from cross-stratified to massive relate to dilute PDCs with a basal boundary evolving from tractional to granular due to changes in deposition rate (see Douillet et al. 2013). The intercalated coarse and massive layers are related to granular-dominated boundary zones and their coarser grain size compared to the cross-stratified bedsets also suggests that also the transport system was different, not only the boundary processes. We thus interpret those layers as deposits from dense pyroclastic flows that overflowed the poorly defined valleys of the proximal zone (Fig. 11).

The source of momentum likely comes from acceleration on the steep slopes because "visual observation indicates that the PDCs were formed under conditions of zero, or small, initial velocities" (Kelfoun et al. 2009). Moreover, the wide extent of the sheet-like deposit suggests that momentum could be maintained by the steepness of the flanks close to the repose angles.

Distal cross-stratified facies

The grain size distribution and sedimentary structures of the *D-Xst* facies indicate deposition from turbulent flows with a tractional basal boundary. Moreover, the ash bodies are found on interfluves, commonly on the outer overbank of curves with orientation of DBs aligning with the direction of the thalweg upstream of the curve (zones B, C, E, F, and III). This indicates that inertial effects dominated over gravitational ones, making the flows less susceptible to redirection in response to topography, and suggesting *dilute* flows. DBs in ash body II, III, and C indicate currents initially traveling away from the valley but reorienting to the local topography gradient after a short distance. Thus, even if initially driven by their inertia when overflowing, the parental flows were gravity driven as *density currents* rather than driven by energy acquired from a blast or column collapse. Thus, the *D-Xst* facies was deposited from *turbulent*, *dilute* pyroclastic *density currents* with a basal *tractional boundary*. The occasional gradations into massive, ashy layers indicate that the tractional boundary was sometimes inhibited by high basal clast concentrations due to high deposition rates, but still with a surrounding dilute PDC.

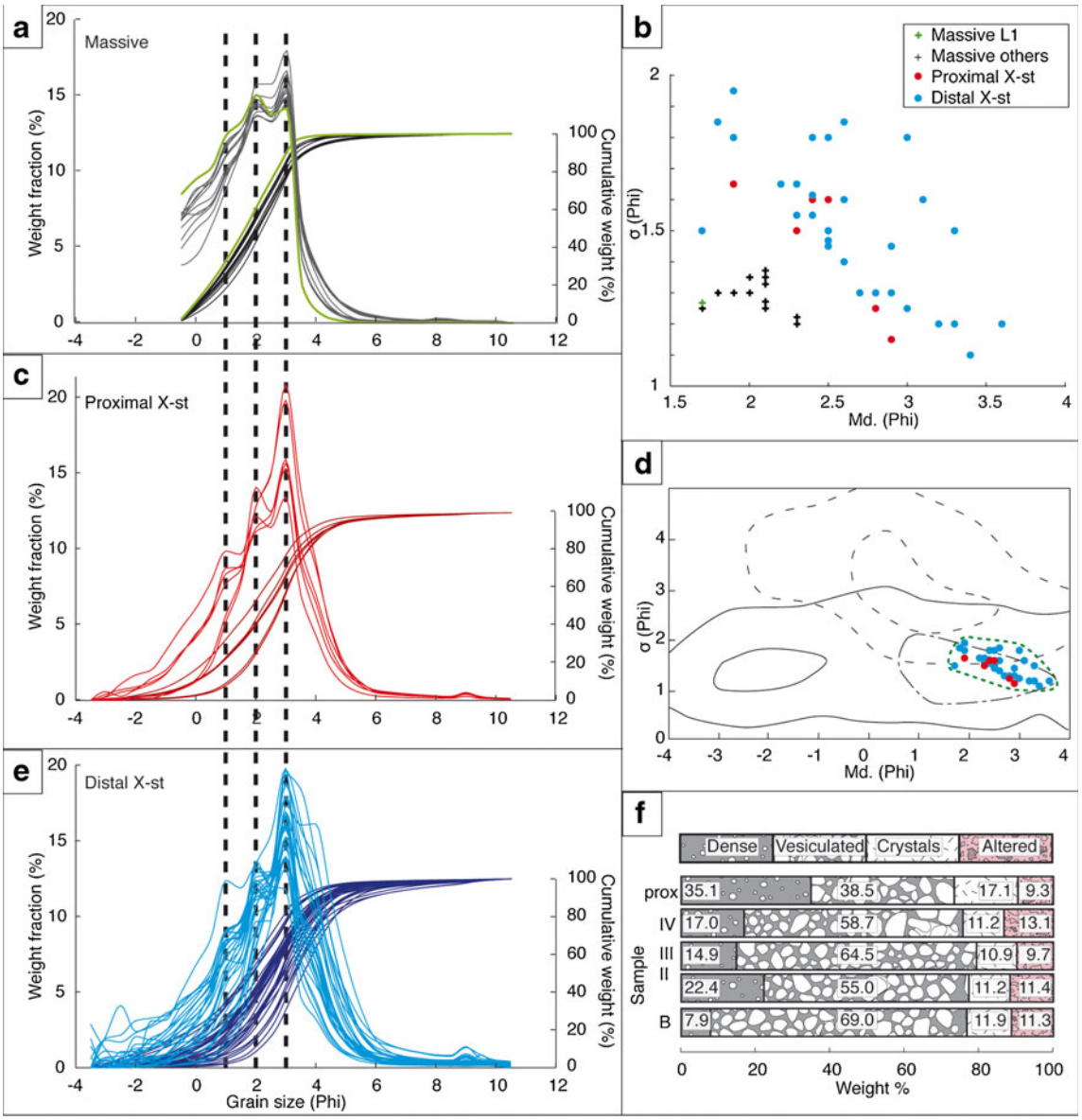

Fig. 10 Sample analysis. **a** Massive, **c** proximal, and **e** distal cross-stratified facies samples. The scale of the frequency curves on left axis, of cumulative weight on right axis. Note the three modes at 1, 2, and 3 phi present in most samples. **b** Median diameter versus sorting coefficient for all samples following the same color coding. **d** Cross-stratified samples plotted with flow (*full lines*) and fall (*dashed lines*) fields of Walker (1971) and "surge" field (*chain line*) of Crowe and Fisher (1973). **f** Componentry analysis within five cross-stratified samples

Origin and deposition of the dilute PDCs

Three main modes are present in the granulometry of most samples. Strikingly, three modes are also present in the fall deposits (though shifted to the fines compared to our dataset), which were interpreted as reflecting a mixed influence from the plume and very dilute and distal co-ignimbrite ash clouds (Eychenne et al. 2012). Within a single current, different modes can be related to different transport mechanisms (Branney and Kokelaar 2002, p. 25) or caused by particle aggregation within the suspended load. We favor an alternative explanation for the presence of the same modes in all facies at Tungurahua. The three modes might be a signature of the fragmentation process rather than the transport process, i.e., a single fragmentation phase was responsible for the flows producing the *Ma*, *P-Xst*, and *D-Xst* facies, implying that the differentiation between dense and dilute parts took place during flow. Otherwise, the fragmentation mechanisms and thus the grain size distributions should be different (Perugini and Kueppers 2012).

Co-ignimbrite plumes have been interpreted to be related to air entrainment at cliffs (Hoblitt 1986; Calder et al. 1997). Fisher (1983) postulated the existence of flow transformations in sediment gravity flows leading to the creation of dilute PDCs from dense flows. At Tungurahua, the steep upper slopes (30°, for dynamic repose angles of 32°) may have enhanced the entrainment of air, subsequently producing the

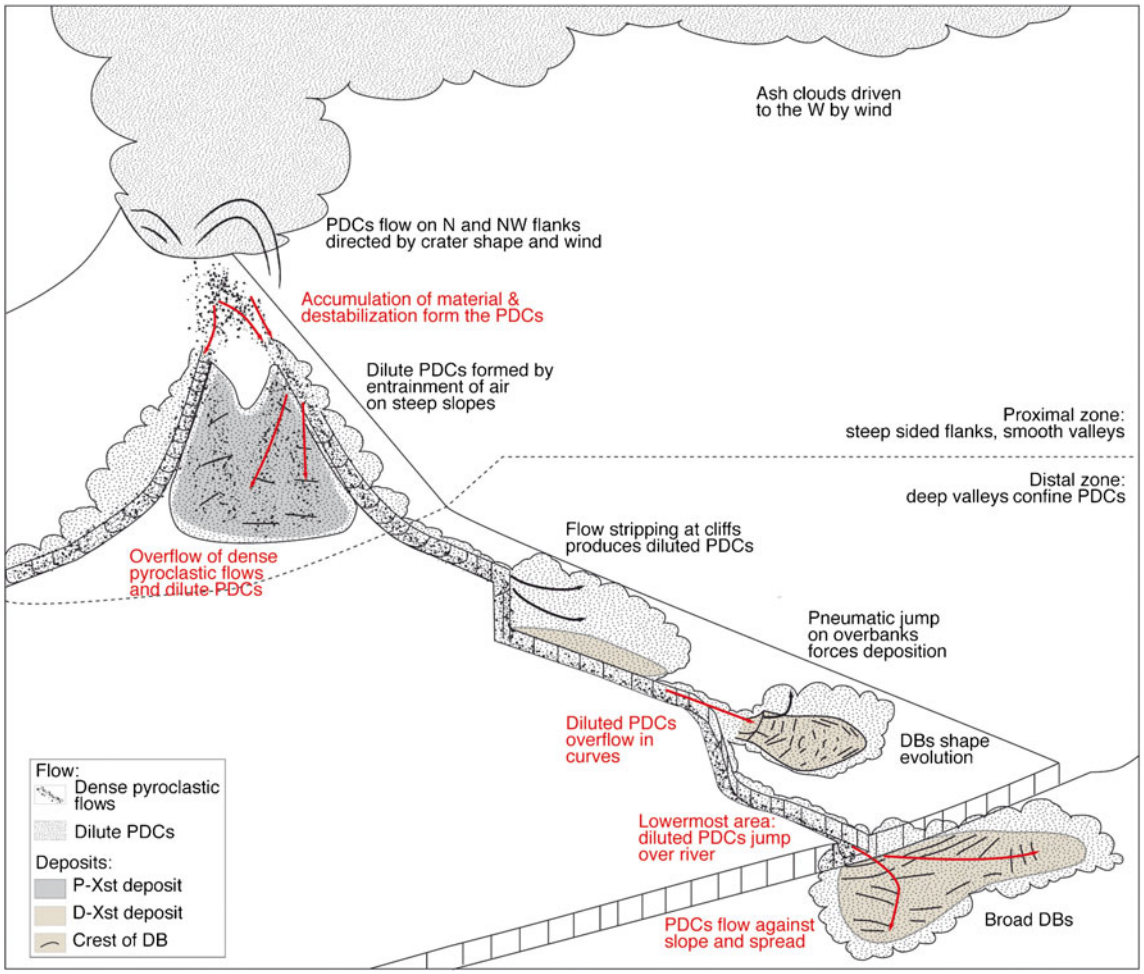

Fig. 11 Interpretative sketch for the formation and deposition of cross-stratified deposits from the August 2006 PDCs at Tungurahua

dilute PDCs responsible for the *P-Xst* facies (Fig. 11). In that case, the gas phase for the dilute PDCs would be mostly ambient air, explaining why trees were only burned when buried in the deposits.

If dilute PDCs had continuously and monotonically emplaced the distal ash bodies, one should observe a monotonic downstream fining trend in the grain size distributions and size decrease of the DBs. Instead, and contrary to most datasets on the size of DBs versus distance from the vent (Wohletz and Sheridan 1979; Sigurdsson et al. 1987; Druitt 1992), the decrease is local for each ash body from its upstream end point (Figs. 6 and 8), while no particular trend is observed with distance to the vent (zone H contains bigger DBs than A, though 2.5 km further away from the vent). Thus, local maximum of energy and/or particle concentration are acting individually for each ash body at their onset rather than a continuous flow. The location of the ash bodies downstream from cliffs further suggests that the latter triggered flow-stripping processes (Fig. 11).

Whether the dilute mode of PDCs existed prior to their encounters with the cliffs is not clear. We do not observe a general decrease of grain size with transport distance, but rather local fining trends depending on distance from the last cliff (Fig. 5e). The dilute PDCs depositing the *D-Xst* facies might thus be created from the dense pyroclastic flows at cliffs by air entrainment and mixing, and be very local features (Fig. 11). As such, they could be termed *diluted* PDCs, and not simply *dilute* PDCs. However, no continuous depositional units are observed and no correlation with the layers observed in the *Ma* outcrops can be done. Interestingly, Andrews and Manga (2012) suggested that the greatest extent of a lamina scales with turbulent eddy dimensions in a dilute PDC: which is 300 m for 125 μm particles and a 30 m/s current, comparable to the extent of the ash bodies.

A higher abundance of vesicular clasts is observed in the samples from the distal Achupashal compared with the proximal ones. This can result from preferential deposition of dense clasts leading to their depletion in distal parts, or can be a consequence of transport abrasion, a process often suggested in PDCs (Dufek and Manga 2008). Indeed, abrasion is more efficient on vesicular clasts (Kueppers et al. 2012). The large number of broken "pancakes" found inside the lobes must have produced vesicular ash by abrasion. These abrasion-induced vesicular ash particles are possibly the reason for the higher

amount of vesicular clasts in the ash fraction in distal zones, given that those dilute flows emanated from the dense.

Whether the dilute PDCs pre-date encounters with the cliffs or not, the local extent of the ash bodies shows that they lacked energy and sufficient particle load after flow stripping, and/or that they rapidly slowed and deposited (as suggested for Unzen by Takahashi and Tsujimoto (2000) and supporting Walker (1984) in his "overall impression that surges—i.e., dilute PDCs—are weak events"). Furthermore, the wedge shape of many ash bodies strikingly resembles sedimentary wedges deposited from experimental particulate density currents at breaks in slopes (Mulder and Alexander 2001) and hydraulic jumps (Sequeiros et al. 2009). The quarter pipe onsets best exemplified in ash body C recorded a strong transition from erosive to depositional currents. Douillet et al. (2013) interpret the associated sedimentary structures as formed by deposition along an intermediate tractional and direct fallout flow boundary. These wedge-shaped ash bodies are located at sharp breaks in slope of the underlying bed. We suggest that these sudden changes from erosive to depositional behavior might be produced by "pneumatic jumps" of the entire dilute PDCs, and the wedge-shaped ash bodies represent their sedimentary signature (Fig. 11). However, no data on the internal stratification of the entire bodies are so far available to settle this genetic question. "Pneumatic jumps" have been suggested for the generation of co-ignimbrite plumes at break in slope for "hot" PDCs (Hoblitt 1986; Calder et al. 1997). Hoblitt (1986) further describe an "ash cloud surge" that overrode the channel walls and shortly thereafter generated a buoyant plume, possibly linked to a "pneumatic jump". Such features might have forced deposition from dilute PDCs at Tungurahua by lowering lateral velocities.

While the long-lived *dilute* vs. local *diluted* nature of the PDCs and deposition through "pneumatic jumps" cannot be resolved, PDCs with a tractional basal boundary, low particle concentration, and very high deposition rates were the parent flows that deposited the distal cross-stratified facies. They were dependent upon the dense pyroclastic flows for provision of energy and supply of particles, and topography has had a significant role in their emplacement, triggering both their overflow and subsequent overbank deposition (Fig. 11).

Acknowledgments We thank our colleagues from Instituto Geofísico, Quito for their valuable information and discussion and Jackie Kendrick for editing the manuscript. The reviews by V Manville, R Cioni, L Guriol, and G Lube were very helpful. We are indebted to the following (partial) funding sources: Alsatian grant BOUSSOLE (GAD); the grant THESIS from the Elite Network of Bavaria (GAD); Deutsche Forschungsgemeinschaft grant KU2689/2-1 (GAD and UK), the Deutsche Forschungsgemeinschaft grant LA 2651/1-1 (FG, JBH, UK, YL); a Research Professorship (LMUexcellent) of the Bundesexzellenzinitiative (DBD); and an advanced grant from the European Research Council–EVOKES 247076 (DBD).

References

Abdurachman EK, Bourdier JL, Voight B (2000) Nuees ardentes of 22 November 1994 at Merapi volcano, Java, Indonesia. J Volc Geotherm Res 100(1–4):345–361

Andrews BJ, Manga M (2012) Experimental study of turbulence, sedimentation, and coignimbrite mass partitioning in dilute pyroclastic density currents. J Volc Geotherm Res 225:30–44

Baines PG (1998) Topographic effects in stratified flows. Cambridge University Press, Cambridge, p 500

Barba D, Arellano S, Ramón P, Mothes P, Alvarado A, Ruiz G, Troncoso L (2006) Cronología de los eventos eruptivos de Julio y agosto del 2006 del volcán Tungurahua. Resumen extendido de las 6tas. Jornadas en Ciencias de la Tierra. Ecuador, DG-EPN, 177–180

Barber CB, Dobkin DP, Huhdanpaa HT (1996) The quickhull algorithm for convex hulls. ACM Trans Math Softw 22(4):469–483

Boudon G, Camus G, Gourgaud A, Lajoie J (1993) The 1984 nuées-ardente deposits of Merapi volcano, Central Java, Indonesia: stratigraphy, textural characteristics and transport mechanisms. Bull Volcanol 55:327–342

Branney MJ, Kokelaar P (2002) Pyroclastic density currents and the sedimentation of ignimbrites. Geological Society Memoir no 27, London, p 143

Brissette FP, Lajoie J (1990) Depositional mechanics of turbulent nuées ardentes (surges) from their grain sizes. Bull Volcanol 53:60–66

Burgisser A, Bergantz GV (2002) Reconciling pyroclastic flow and surge: the multiphase physics of pyroclastic density currents. Earth Planet Sci Lett 202:405–418

Calder ES, Sparks RSJ, Woods AW (1997) Dynamics of co-ignimbrite plumes generated from pyroclastic flows of Mount St. Helens (7 August 1980). Bull Volcanol 58:432–440

Calder ES, Sparks RSJ, Gardeweg MC (2000) Erosion, transport and segregation of pumice and lithic clasts in pyroclastic flows inferred from ignimbrite at Lascar Volcano, Chile. J Volc Geotherm Res 104: 201–235

Charbonnier SJ, Gertisser R (2008) Field observations and surface characteristics of pristine block-and-ash flow deposits from the 2006 eruption of Merapi Volcano, Java, Indonesia. J Volc Geotherm Res 177:971–982

Cole PD (1991) Migration direction of sand wave structures in pyroclastic-surge deposits: implications for depositional processes. Geology 19:1108–1111

Cole PD, Calder ES, Druitt TH, Hoblitt R, Robertson R, Sparks RSJ, Young SR (1998) Pyroclastic flows generated by gravitational instability of the 1996–97 lava dome of Soufriere Hills Volcano, Montserrat. J Geophys Res Lett 25(18):3425–3428

Cole PD, Calder ES, Sparks RSJ, Clarke AB, Druitt TH, Young SR, Herd RA, Harford CL, Norton GE (2002) Deposits from dome-collapse and fountain-collapse pyroclastic flows at Soufriere Hills Volcano, Montserrat. In: Druitt TH, Kokelaar BP (eds) The eruption of Soufriere Hills Volcano, Montserrat, from 1995 to 1999, vol 21. Geological Society London, Memoir, pp 231–262

Crowe BM, Fisher RV (1973) Sedimentary structures in base-surge deposits with special reference to cross-bedding, Ubehebe Craters, Death Valley. California Geol Soc Amer Bull 84:663–682

Cressie N (1993) Statistics for spatial data Wiley series in probability and mathematical statistics: applied probability and statistics. Wiley, New York, Revised reprint of the 1991 edition

Dellino P, Isaia R, La Volpe L, Orsi G (2004) Interaction between particles transported by fallout and surge in the deposits of the Agnano-Monte Spina eruption (Campi Flegrei, Southern Italy). J Volc Geotherm Res 133:193–210

Douillet GA, Pacheco DA, Kueppers U, Letort J, Tsang-Hin-Sun È, Bustillos J, Hall M, Ramón P, Dingwell DB (2013) Dune bedforms produced by dilute pyroclastic density currents from the August

2006 eruption of Tungurahua volcano, Ecuador. Bull Volcanol 75:762. doi:10.1007/s00445-013-0762-x

Drazin PG (2002) Introduction to hydrodynamic stability. Cambridge texts in applied mathematics. Cambridge University Press, Cambridge, 258 pages

Druitt TH (1992) Emplacement of the 18 May 1980 lateral blast deposit ENE of Mount St. Helens, Washington. Bull Volcanol 54:554–572

Druitt TH (1996) Pyroclastic density currents. In: Gilbert JS, Sparks RSJ (eds) The physics of explosive volcanic eruptions, vol. 145. Geological Society, London, pp 145–182, Special Publications

Dufek J, Manga M (2008) In situ production of ash in pyroclastic flows. J Geophys Res 113, B09207

Eychenne J, Lepennec JL, Troncoso L, Gouhier M, Nedelec JM (2012) Causes and consequences of bimodal grain-size distribution of tephra fall deposited during the August 2006 Tungurahua eruption (Ecuador). Bull Volcanol 74(1):187–205

Félix G, Thomas N (2004) Relation between dry granular flow regimes and morphology of deposits: formation of levées in pyroclastic deposits. Earth Planet Sci Lett 221:197–213

Fildani A, Normark WR, Kostik S, Parker G (2006) Channel formation by flow stripping: large-scale scour features along the Monterey East Channel and their relation to sediment waves. Sedimentology 53: 1265–1287

Fisher RV (1983) Flow transformations in sediment gravity flows. Geology 11:273–274

Fisher RV (1995) Decoupling of pyroclastic currents: hazards assessments. J Volc Geotherm Res 66:257–263

Freundt A, Schmincke HU (1985) Lithic enriched segregation bodies in pyroclastic flow deposits of Laacher See volcano (East Eifel, Germany). J Volc Geotherm Res 25:193–224

Folk RL (1964) A review of grain size parameters. Sedimentology 6:73–93

García M, Parker G (1989) Experiments on hydraulic jumps in turbidity currents near a canyon-fan transition. Science 245:393–396

García MH (1993) Hydraulic jumps in sediment-driven bottom currents. J Hydraul Eng 119(10):1094–1117

Gardner JE, Burgisser A, Stelling P (2007) Eruption and deposition of the Fisher Tuff (Alaska): evidence for the evolution of pyroclastic flows. J Geology 115(4):417–435

Giannetti B, Luongo G (1994) Trachyandesite scoria-flow and associated trachyte pyroclastic flow and surge at Roccamonfina Volcano (Roman Region, Italy). J Volc Geotherm Res 59:313–334

Goldstein F (2011) Geological Mapping of the 2006 Pyroclastic Density Current Deposits on Tungurahua Volcano, Ecuador. Diplomkartierung ausgegeben und betreut von Prof. A. Altenbach München, 01. Januar 2011. Ludwig-Maximilians-Universität München. Department für Geo- und Umweltwissenschaften, Sektion Geologie/Paläontologie

Gurioli L, Cioni R, Sbrana A, Zanella E (2002) Transport and deposition of pyroclastic density currents over an inhabited area: the deposits of the AD 79 eruption of Vesuvius at Herculaneum, Italy. Sedimentology 49:929–953

Gurioli L, Zanella E, Pareschi MT, Lanza R (2007) Influences of urban fabric on pyroclastic density currents at Pompeii (Italy): flow direction and deposition (part I). J Geophys Res 112, B05213

Hall ML, Robin C, Beate B, Mothes P, Monzier M (1999) Tungurahua Volcano, Ecuador: structure, eruptive history and hazards. J Volc Geotherm Res 91:1–21

Hall ML, Samaniego P, Le Pennec JL, Johnson JB (2008) Ecuadorian Andes volcanism: a review of Late Pliocene to present activity. J Volc Geotherm Res 176(1):1–6

Hoblitt RP (1986) Observations of the eruptions of July 22 and August 7, 1980, at Mount St. Helens, Washington. U.S.A. Geological survey professional paper 1335

Kelfoun K, Samaniego P, Palacios P, Barba D (2009) Testing the suitability of frictional behaviour for pyroclastic flow simulation by comparison with a well-constrained eruption at Tungurahua volcano (Ecuador). Bull Volcanol 71(9):1057–1075

Kueppers U, Putz C, Spieler O, Dingwell DB (2012) Abrasion in pyroclastic density currents: insights from tumbling experiments. Phys Chem Earth 45–46:33–39

Legros F, Kelfoun K (2000) On the ability of pyroclastic flows to scale topographic obstacles. J Volc Geotherm Res 98:235–241

Lube G, Cronin SJ, Platz T, Freundt A, Procter JN, Henderson C, Sheridan MF (2007) Flow and deposition of pyroclastic granular flows: a type example from the 1975 Ngauruhoe eruption, New Zealand. J Volc Geotherm Res 161:165–186

Lube G, Cronin SJ, Thouret JC, Surono (2011) Kinematic characteristics of pyroclastic density currents at Merapi and controls on their avulsion from natural and engineered channels. Geol Soc Am Bulletin 123(5/6):1127–1140

Macías JL, Espíndola JM, Bursik M, Sheridan MF (1998) Development of lithic-breccias in the 1982 pyroclastic flow deposits of El Chichón Volcano, Mexico. J Volc Geotherm Res 83:173–196

Moore JG (1967) Base surge in recent volcanic eruptions. Bull Volcanol 30(1):337–363

Mulder T, Alexander J (2001) Abrupt change in slope causes variation in the deposit thickness of concentrated particle driven density currents. Mar Geol 175:221–235

Normark WR, Piper DJW, Posamentier H, Pirmez C, Migeon S (2002) Variability in form and growth of sediment waves on turbidite channel levees. Mar Geol 192:23–58

Otto GH (1939) A modified logarithmic probability graph for the interpretation of mechanical analysis of sediments. J Sed Petrol 9:62–76

Perugini D, Kueppers U (2012) Fractal analysis of experimentally generated pyroclasts: a tool for volcanic hazard assessment. Acta Geophysica 60(3):682–698

Piper DJW, Normark WR (1983) Turbidite depositional patterns and flow characteristics, Navy Submarine Fan, California Borderland. Sedimentology 30:681–694

Prather BE (2003) Controls on reservoir distribution, architecture and stratigraphic trapping in slope settings. Mar Pet Geol 20:529–545

Samaniego P, Le Pennec JL, Barba D, Hall M, Robin C, Mothes P, Yepes H, Troncoso L, Jaya D (2008) Mapa de los peligros potenciales del volcán Tungurahua. (Esc. 1/50.000), 3ra Edición, Edit. IGM-IG/EPN-IRD, Quito, Ecuador

Samaniego P, Le Pennec JL, Robin C, Hidalgo S (2011) Petrological analysis of the pre-eruptive magmatic process prior to the 2006 explosive eruptions at Tungurahua volcano (Ecuador). J Volc Geotherm Res 199(1–2):69–84

Sandwell DT (1987) Biharmonic spline interpolation of GEOS-3 and SEASAT Altimeter Data. Geophys Res Lett 14(2):139–142

Sarocchi D, Sulpizio R, Macías JL, Saucedo R (2011) The 17 July 1999 block-and-ash flow (BAF) at Colima Volcano: new insights on volcanic granular flows from textural analysis. J Volc Geotherm Res 204:40–56

Saucedo R, Macias JL, Bursik MI, Mora JC, Gavilanes JC, Cortes A (2002) Emplacement of pyroclastic flows during the 1998–1999 eruption of Volcan de Colima, Mexico. J Volc Geotherm Res 117: 129–153

Schmincke HU, Fisher RV, Waters AC (1973) Antidune and chute-and-pool structures in the base surge deposits of the Laacher See area, Germany. Sedimentology 20:553–574

Sequeiros OE, Spinewine B, García MH, Beaubouef RT, Sun T, Parker G (2009) Experiments on wedge-shaped deep sea sedimentary deposits in minibasins and/or on channel levees emplaced by turbidity currents. Part I: Documentation of the flow. J Sed Res 79: 593–607

Sigurdsson H, Carey SN, Fisher RV (1987) The 1982 eruption of E1 Chichón volcano, Mexico (3): physical properties of pyroclastic surges. Bull Volcanol 49:467–488

Sneed SD, Folk FL (1958) Pebbles in the lower Colorado River, Texas, a study of particle morphogenesis. J Geology 66(2):114–150

Sparks RSJ (1976) Grain size variations in ignimbrites and implications for the transport of pyroclastic flows. Sedimentology 23: 147–188

Sulpizio R, De Rosa R, Donato P (2008) The influence of variable topography on the depositional behaviour of pyroclastic density currents: the examples of the Upper Pollara eruption (Salina Island, southern Italy). J Volc Geotherm Res 175:367–385

Sulpizio R, Bonasia R, Dellino PF, Mele D, Di Vito MA, La Volpe L (2010) The Pomici di Avellino eruption of Somma–Vesuvius (3.9 ka BP). Part II: sedimentology and physical volcanology of pyroclastic density current deposits. Bull Volcanol 72:559–577

Takahashi T, Tsujimoto H (2000) A mechanical model for Merapi-type pyroclastic flow. J Volc Geotherm Res 98:91–115

Talbot JP, Self S, Wilson CJN (1994) Dilute gravity current and rain-flushed ash deposits in the 1.8 ka Hatepe Plinian deposit, Taupo, New Zealand. Bull VolcanoI 56:538–551

Valentine GA (1987) Stratified flow in pyroclastic surges. Bull Volcanol 49:616–630

Valentine GA, Giannetti B (1995) Single pyroclastic beds deposited by simultaneous fallout and surge processes: Roccamonfina volcano, Italy. J Volc Geotherm Res 64:129–137

Walker GPL (1971) Grain-size characteristics of pyroclastic deposits. J Geology 79:619–714

Walker GPL, Wilson CJN, Froggatt PC (1981) An ignimbrite veneer deposit: the trail-marker of a pyroclastic flow. J Volc Geotherm Res 9:409–421

Walker GPL (1984) Characteristics of dune-bedded pyroclastic surge bedsets. J Volc Geotherm Res 20:281–296

Waltham D (2004) Flow transformations in particulate gravity currents. J Sed Res 74(1):129–134

Wilson CNJ, Hildreth W (1998) Hybrid fall deposits in the Bishop Tuff, California: a novel pyroclastic depositional mechanism. Geology 26:7–10

Wohletz KH, Sheridan MF (1979) A model of pyroclastic surge. Geol Soc Am Special Paper 180:177–194